IEEE Access
Multidisciplinary ⋮ Rapid Review ⋮ Open Access Journal

Received April 13, 2022, accepted April 25, 2022, date of publication April 28, 2022, date of current version May 5, 2022.

*Digital Object Identifier 10.1109/ACCESS.2022.3170896*

# Performance Enhancement of the IPMSM for HEV Applications Using Grain-Oriented Electrical Steel and Design Optimization

**JI-CHANG SON[1], JI-YEON KIM[2], JAE-WAN CHOI[2], DONG-KUK LIM[1], AND HAN-KYEOL YEO[3]**

[1]Department of Electrical, Electronic, and Computer Engineering, University of Ulsan, Ulsan 44610, Republic of Korea
[2]Department of Advanced Electrification Engineering Design Team, Hyundai Motor Company, Hwaseong 18280, Republic of Korea
[3]Division of Electrical and Electronic Engineering, The University of Suwon, Hwaseong 18323, Republic of Korea

Corresponding author: Han-Kyeol Yeo (yeohankyeol@gmail.com)

This work was supported by the Regional Innovation Strategy (RIS) through the National Research Foundation of Korea (NRF) by the Ministry of Education (MOE) under Grant 2021RIS-003.

**ABSTRACT** This paper proposes a method for enhancing the performance of an interior permanent magnet synchronous motor (IPMSM) using grain-oriented electrical steel (GO) and design optimization. As the GO has superior magnetic characteristics in the rolling direction, the GO is applied to the stator teeth to increase the torque and reduce the iron loss of the IPMSM. However, such an approach leads to higher saturation on the core, resulting in worse pulsation characteristics. To handle with pulsation problem on the IPMSM, design optimization is conducted. In this paper, the interpolation multi-objective robust optimization algorithm (IMROA) was proposed. The IMROA can reduce the calculation time by interpolating the objective region and utilizing a stepwise sampling strategy. Moreover, the IMROA considers the robustness of the found solution and can derive a robust global solution that has robustness on the manufacturing tolerance and deformation during the operation and prevents unexpected results on the IPMSM.

**INDEX TERMS** Design optimization, grain-oriented electrical steel, hybrid electric vehicle, interior permanent magnet synchronous motor, robustness, surrogate model.

## I. INTRODUCTION

Electric vehicles (EVs) and hybrid electric vehicles (HEVs) have rapidly developed in recent years and are commonly regarded as one of the promising solutions for emission reduction and energy conservation [1]–[3]. From the environmental standpoint, the EV, which is only driven by an electric motor, seems to be the better option. However, EVs still have problems with long charging times and the expensive cost of establishing a charging infrastructure, and further research and development is needed for increasing the battery capacity and efficiency to extend their driving range [4]–[7].

Unlike EVs, the HEV is a vehicle using both an internal combustion engine (ICE) and an electric motor, which is called as hybrid power source [8]. As a result, the HEV could optimize the power distribution and maximize the energy efficiency by using the motor at the starting sequence and lower-speed region and using the engine in the high-speed operating region. Therefore, HEVs are considered as solution for increasing energy efficiency without compromising vehicle performance [9], [10].

For the traction motors, which is one of the major components of the HEV application, high efficiency, high power density, and wide speed range control is required, and therefore, permanent magnet synchronous motors (PMSMs) are widely used [11], [12]. Especially, interior PMSMs (IPMSMs) are suitable for traction motor as the magnets are embedded inside the rotor core and have superior mechanical stability. Moreover, as the IPMSMs have both magnet torque and reluctance torque, high torque density can be obtained [13].

When designing the traction motor, various performance factors should be considered. Designed motor should have robustness against the manufacturing tolerances and deformation during operation to avoid unexpected results, and the pulsation component of the torque waveform that can affect the driving comfort and control stability should be small [14]–[16]. In addition, the output characteristics of the motor

The associate editor coordinating the review of this manuscript and approving it for publication was Shihong Ding.

should be improved, because the increased torque enables reducing the stacking length and downsizing the motor or improves the thermal characteristic by reducing the input current.

In this paper, grain-oriented electrical steel (GO) is applied to an IPMSM to acquire torque improvement. Especially, as the magnetic characteristics of the GO vary according to the angle of the flux, the GO is partially applied to the stator teeth, where the direction of the flux path is uniform, and the effect of the GO can be maximized [17].

In addition, design optimization was conducted to further improve various performances of the IPMSM, including the torque pulsation characteristic. The interpolation multi-objective robust optimization algorithm (IMROA) was newly proposed for the design optimization of the IPMSM. The IMROA can reduce the number of function calls to convergence by utilizing the interpolated objective region. Moreover, by considering the robustness of the found solutions, the optimal design with robustness, while improving the various performances, can be obtained.

## II. TORQUE ENHANCEMENT OF THE IPMSM USING GRAIN-ORIENTED ELECTRICAL STEEL

In this section, the GO is applied to the target IPMSM model for the HEV application for the purpose of improving the performance of the motor. The characteristic curves of the non-grain-oriented electrical steel (NO) and GO are compared, and the specifications of the target IPMSM are introduced. Through the magnetic flux path analysis of the IPMSM obtained by finite element analysis (FEA), the stator part that maximizes the effect of the GO was selected. Finally, by comparing the FEA results of the NO model and the GO applied model, the superiority of the GO was confirmed.

### A. MAGNETIC CHARACTERISTIC OF THE GRAINORIENTED ELECTRICAL STEEL

Electrical steel can be classified into two categories according to the magnetic anisotropy characteristics; one is NO, and the other is GO. The magnetic characteristics of the former are uniform regardless of the direction of the magnetic flux flowing through the NO. Therefore, NO has been widely used for the core material of the rotation machine, such as the motor, that the direction of the magnetic flux of the core changes according to the position of the rotor or the instantaneous input current of each phase [18].

On the other hand, the later has strong magnetic anisotropy, and the magnetic characteristic varies according to the direction of the magnetic flux to the rolling direction of the GO. The GO shows superior magnetic characteristics when a direction of the magnetic flux matches the rolling direction. However, it shows inferior characteristics when the flux is perpendicular to the rolling direction, which is the transverse direction [19]. Due to such magnetic orientation characteristics, the GO is suitable for enhancing the performance of electrical machines with a uniform flux path, especially transformers [20].

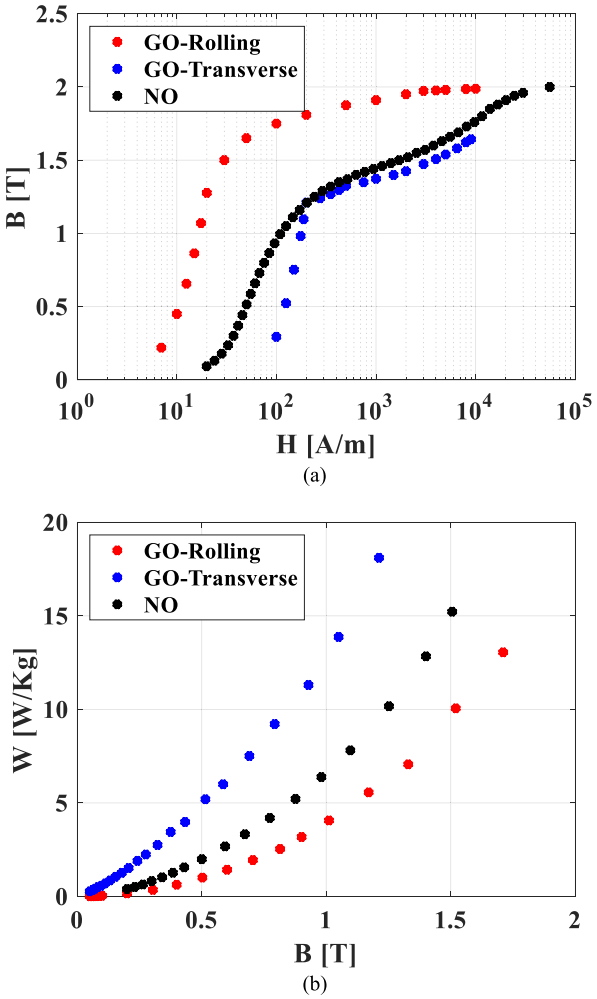


**FIGURE 1.** Magnetic characteristics of the NO and GO. (a) B-H curve. (b) B-W curve.

The magnetic characteristics of the NO and GO are compared in Fig. 1. The compared materials are 35JN230 and 35ZH135 for the NO and GO, respectively. Fig. 1(a) and Fig. 1(b) show the magnetic flux density-magnetic field curve (B-H curve) and the magnetic flux density-iron loss density (B-W curve) of the NO and GO. As shown in Fig. 1, the GO shows superior performance in the rolling direction, and inferior performance in the transverse direction compared with the NO. Therefore, in order to improve the performance of the IPMSM, it is critical to properly place the GO where the magnetic flux flows in the rolling direction.

### B. TARGET IPMSM FOR HEV APPLICATION

The IPMSM is a suitable type of motor for the traction motor for the HEV applications, as the IPMSM satisfies the requirements on high torque density, superior power factor, and high efficiency [21]–[24]. The target model benchmarked the model of the [25]. The specifications and requirements of the IPMSM are tabulated in Table 1, and configuration of the target model is shown in Fig. 2.

To determine where to apply the GO, FEA is conducted to confirm the magnetic flux path of the target model. The JMAG, which is the commercial FEA analysis tool, is used to analyze the load and no-load conditions of the IPMSM. Fig. 3 shows the load condition flux path on the core according to the rotor position. The flux path on the rotor core is uniform regardless of the rotor position. However, the rotor is not suitable for GO application, as the flux path highly relies on the array of the magnet, and there is a mechanical stability problem at high-speed rotation.

**TABLE 1. Specifications and requirements of the target IPMSM.**

| Specifications | Value |
|---|---|
| Pole / slot number | 16 / 24 |
| Stator inner / outer diameter [mm] | 202 / 280 |
| Rotor inner / outer diameter [mm] | 172 / 200 |
| Airgap [mm] | 1.0 |
| Bridge [mm] | 1.2 |
| Stacking length [mm] | 70 |
| Core material | 35JN230 |
| Current density [$A_{rms}/mm^2$] | 13.0 |
| **Requirements** | **Value** |
| Rated output [kW] | 57.2 |
| Rated torque [Nm] | 260 |
| Rated speed [RPM] | 2100 |

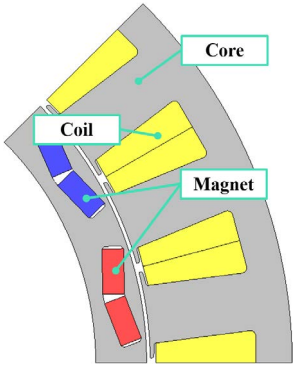


**FIGURE 2. Configuration of the target IPMSM.**

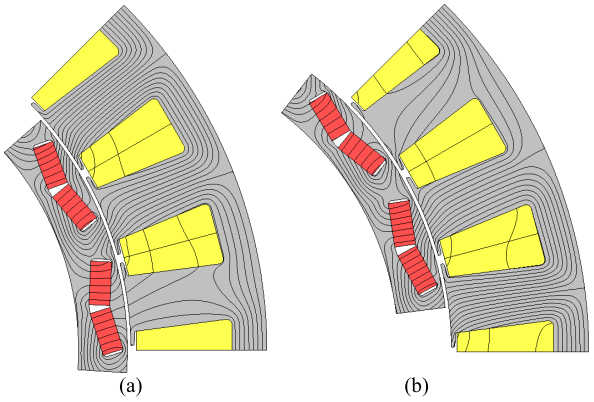


**FIGURE 3. Flux path on the core according to the rotor position. (a) At a mechanical degree of 0. (b) At a mechanical degree of 11.25.**

The stator core can be divided into two parts, the yoke and the teeth. The flux path on the yoke part varies greatly depending on the position of the rotor. However, the flux path on the teeth part is constant in the radial direction regardless of the rotor position. Therefore, when the GO is applied to the teeth part, magnetic flux flows in the rolling direction of the core, and the effect of improving the performance of the motor can be high, which can be confirmed from Fig. 1.

### C. PERFORMANCE COMPARISON OF THE NO MODEL AND THE GO MODEL

Based on the magnetic flux path analysis results of the NO model, the GO is applied to the stator teeth part to enhance the performance of the IPMSM. The configurations of the NO and GO models are shown in Fig. 4. The GO model has a connection part at the boundary of the NO and GO, so that the teeth can be fixed to the attraction between the rotor and the stator.

The load and no-load condition analysis using FEA is conducted, and the detailed analysis results and comparison are tabulated in Table 2. In detail, for the no-load condition, the iron loss of the GO model was 25.40% reduced compared with the NO model. The line to line back-electromotive force (B-EMF) was 0.53% increased, the B-EMF total harmonic distortion (THD) was 5.56% reduced, and the cogging torque was 7.42% increased. For the load condition, the average torque was 5.50% increased, the iron loss was 9.64% reduced, and the efficiency was 0.25% increased. However, the torque ripple was 43.89% increased.

The torque increase and iron loss decrease effect of applying the GO was confirmed by the results in Table 2. Fig. 5 shows the magnetic flux density contour plots of the NO and GO models at the load and no-load condition. As shown in Fig. 1(a), the GO has superior B-H curve characteristics in the rolling direction. Therefore, the GO model shows higher saturation (Fig. 5(c)) compared with the NO model (Fig. 5(a)), and the reason for the torque increase was higher saturation on the stator. However, due to the severe saturation on the core, the torque ripple of the GO model was 43.89% higher compared with the NO model. In this paper,

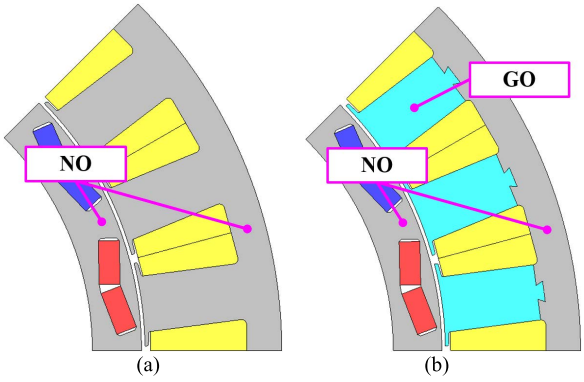


**FIGURE 4. Configuration of the conventional NO model and the GO model. (a) NO model. (b) GO model.**

**TABLE 2. Analysis results and comparison of the NO and GO models.**

| No-load | NO model | GO model | Comparison |
|---|---|---|---|
| B-EMF [$V_{rms}$] | 158.69 | 159.83 | +0.53 [%] |
| B-EMF THD [%] | 12.24 | 11.56 | -5.56 [%] |
| Cogging torque [Nm] | 10.33 | 11.30 | +7.42 [%] |
| Iron loss [W] | 174.96 | 130.53 | -25.40 [%] |
| **Load** | **NO model** | **GO model** | **Comparison** |
| Average torque [Nm] | 263.19 | 277.66 | +5.50 [%] |
| Torque ripple [%] | 14.40 | 20.72 | +43.89 [%] |
| Iron loss [W] | 456.39 | 412.41 | -9.64 [%] |
| Efficiency [%] | 96.40 | 96.65 | +0.25 [%] |

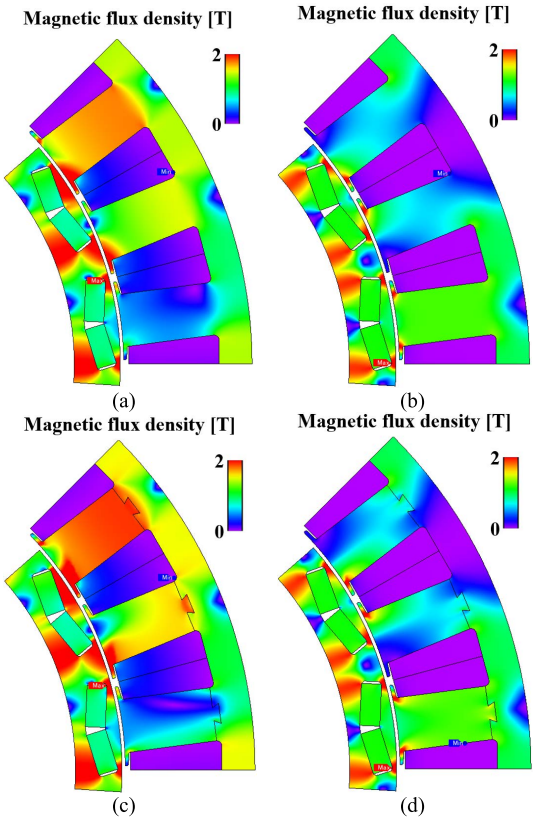


**FIGURE 5. Magnetic flux density contour plot. (a) NO model, load. (b) NO model, no-load. (c) GO model, load. (d) GO model, no-load.**

design optimization is conducted to handle the pulsation problem.

## III. OPTIMAL DESIGN OF THE IPMSM USING IMROA

For the traction motors of the HEVs, high pulsation characteristics can cause mechanical vibration and acoustic noise in the vehicles [26]. Such torque ripple problems can be solved through the optimal design of the motor structure. Since the FEA, which requires a huge computational burden, is required to analyze the motor, an optimization algorithm that can find an exact solution within a small number of function calls is required. However, when the designed motor is manufactured, expected performances may not be achieved due to manufacturing tolerance issues and the deformation of the motor [27]. In this paper, to avoid the influence of uncertainty of design parameters and to ensure the robustness of the solution, the novel optimization algorithm, that finds all the solutions including global and local solutions and checks the robustness, is proposed.

### A. INTERPOLATION MULTI-OBJECTIVE ROBUST OPTIMIZATION ALGORITHM

The optimal design of the electrical machine is a multi-objective optimization problem as the various aspects, such as torque, torque ripple, and THD, of the motor should be considered. One of the methods of considering multi-objectives is the weighted sum method (WSM), which multiplies the assigned weight of each objective and adds them together. The IMROA utilizes the WSM and can consider multi-objectives as a single objective.

To reduce the number of function calls, the IMROA utilizes a surrogate model interpolated by samples on the problem domain such that computation time can be saved compared with standard approaches [28]. The flow chart of the IMROA is shown in Fig. 6. The IMROA effectively adjusts the number of generated samples using a stepwise sampling strategy that consists of peripheral search sampling (PSS), regional search sampling (RSS), and robust test sampling (RTS).

The PSS generates samples that are spread out while maintaining randomness throughout the entire problem domain. In addition, PSS repeatedly adds the sample at the farthest

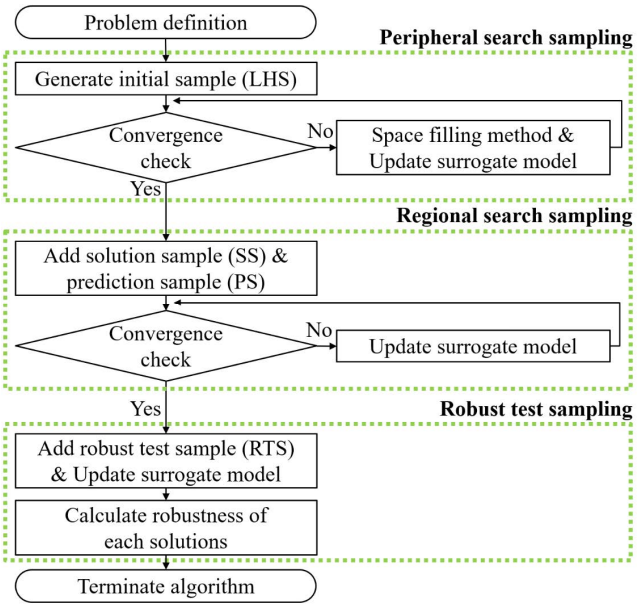


**FIGURE 6. Flow chart of the IMROA.**

point from the existing samples until all local solutions are roughly found. In RSS, samples are added considering the distances of the existing samples and moving direction of the solutions of surrogate model at each generation. At the end of the algorithm, when the solutions are obtained, RTS is added to test the tolerance for each variable, and the robust optimal solution is determined.

#### 1) PERIPHERAL SEARCH SAMPLING

At the beginning of the IMROA, PSS is conducted to roughly interpolate the entire problem domain without missing local solutions. Firstly, the initial samples are generated using the Latin hypercube sampling method, which is an efficient sampling method that generates uniformly distributed samples with randomness [29], [30]. The objective region is interpolated using the generated initial samples. Then, to find all the solutions without omission, a new sample is added at the farthest point from the existing samples. The process is repeated until the number of the found solutions in the interpolated region does not change.

#### 2) REGIONAL SEARCH SAMPLING

After the PSS, RSS is executed to improve the accuracy of the found solutions and accelerate the convergence to the solution. The RSS adds two samples near each solution, the solution sample (SS) and the prediction sample (PS). When the surrogate model is updated in a new generation, the SS is added on each solution of the surrogate model. With the SS, as generations are repeated, the accuracy of the surrogate model can be improved, especially near the actual solution.

The PS is added on the nearest contour line surrounding the solution of the surrogate model. To determine the position of PS, the coordinates of the solutions of the current and previous generation surrogate models are used.

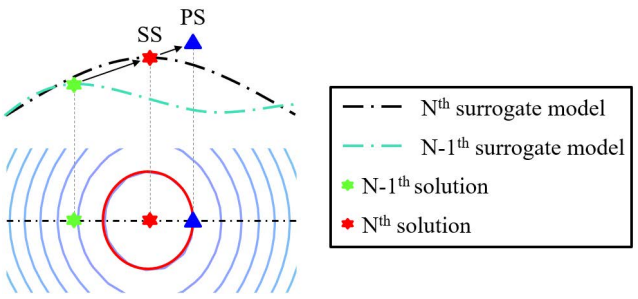


**FIGURE 7.** Conceptual schematic of the RSS.

Fig. 7 shows the principle of the PS. The green and black dashed lines are surrogate models of the previous and current iteration. On the contour plot, which indicates the current surrogate model, the solution of the surrogate model is moved to the (+) direction. Therefore, the position of the actual solution is likely to be located to the right of the solution of the current surrogate model. Accordingly, the PS is generated on the blue triangle, which is in the (+) direction on the red circle line.

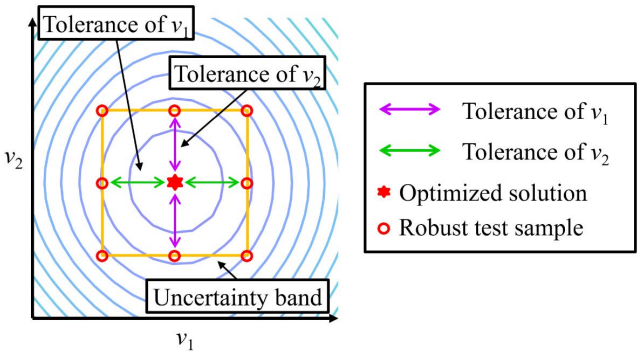


**FIGURE 8.** Conceptual schematic of the RTS.

#### 3) ROBUST TEST SAMPLING

When enough iterations have passed and all the solutions are found by PSS and RSS, RTS is conducted to determine the robust optimal solution. Fig. 8 shows an example of the robustness test. The red star ($v_{1os}$, $v_{2os}$) is the optimized solution of the algorithm. Considering the manufacturing tolerance of each variable, the orange line represents the uncertainty band of the solution, and samples are added at the red points ($v_{1os}\pm dv_1$, $v_{2os}\pm dv_2$). For the maximization problem, among the red points, the point with the minimum function value, which is the same as the worst case of the uncertainty band, becomes a robust solution. Finally, the point with the largest value among other robust solutions is selected as the robust optimal solution.

### *B. PERFORMANCE VERIFICATION AT THE MATHEMATICAL TEST FUNCTIONS*

To verify the superiority of the proposed algorithm, three multimodal optimization algorithms are applied to the optimization of two mathematical test functions, and the objective regions of each test function are shown in Fig. 9. The blue and red dots represent the global solution and robust optimal solution, respectively. Two test functions can be expressed as

$$f = \sum_{i=1}^{N} \frac{b_i}{1 + [(x - x_i)^2 + (y - y_i)^2]/a_i} \tag{1}$$

where $N$ is the number of solutions, $(x_i, y_i)$ is the coordinates of the $i^{\text{th}}$ solution, $a_i$ and $b_i$ are the constant determines the width and height of the solution. The detailed information of each test function is as follows.

**Test function 1**

$N = 9$

$a_i = [40, 40, 10, 40, 100, 40, 40, 40, 40]$

$b_i = [20, 10, 30, 20, 27, 10, 15, 15, 20]$

$(x_i, y_i) = [(40, 40), (40, -35), (40, 5), (0, 40), (10, -30), (15, 10), (-30, 45), (-45, -40), (-35, -5),]$

**Test function 2**

$N = 5$

$a_i = [100, 100, 10, 200, 100]$

$b_i = [11, 8, 20, 17, 10]$

$(x_i, y_i)$ = [(30, 30), (−30, −30), (−30, 30), (0, 0), (30, −30)]

The robust niching genetic algorithm (RNGA) and the robust immune algorithm (RIA), which are widely known optimization algorithms, are used. The robust test is equally applied after both algorithms are terminated.

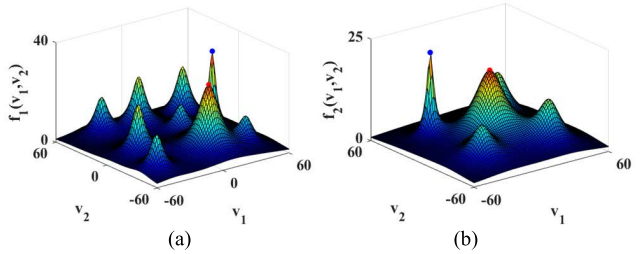


**FIGURE 9.** Mathematical test functions. (a) Test function 1 with 9 solutions. (b) Test function 2 with 5 solutions.

**TABLE 3.** Performance comparison of IA, NGA, and IRMOA.

| Test Function 1 [9 peaks] | Number of function calls [EA] | Convergence rate [%] |
|---|---|---|
| RIA | 2641.0 | 99.59 |
| RNGA | 1927.0 | 97.79 |
| IRMOA | 318.7 | 99.76 |
| Test Function 2 [5 peaks] | Number of function calls [EA] | Convergence rate [%] |
| RIA | 1605.0 | 99.83 |
| RNGA | 1711.0 | 98.63 |
| IRMOA | 166.0 | 99.35 |

The criteria for performance comparison are the convergence rate, which is the ratio of the found solution to the actual robust solution, and the number of function calls to converge to the robust optimal solution. The test is repeated 100 times and the average test result is listed in Table 3.

Each algorithm is set to terminate when all solutions are found, so that the convergence rates of all tests are over 99%. In the case of test function 1, the number of function calls of the IMROA is reduced by 87.9% and 83.5% compared with RIA and RNGA, respectively. For test function 2, the reduction rate of the number of function calls of IMROA is 89.7% and 90.3%. Therefore, the superiority of the proposed IMROA is verified by comparing the test results.

### C. DESIGN OPTIMIZATION OF THE IPMSM FOR HEV APPLICATION USING IMROA

The verified IMROA is applied to design optimization of the IPMSM GO model, which shows high pulsation characteristics. The design variables are shown in Fig. 10 and are selected as the pole arc to pole pitch ratio (*alpha*) and the angle of the magnet ($m_\theta$), as the torque ripple varies according to the shape of the magnet placement [31], [32].

The considered objectives of the optimization were average torque, torque ripple, B-EMF THD, and cogging torque. After obtaining the initial samples, each objective value is normalized between 0 to 1. The normalized objective value can be calculated as

$$obj_{norm\_i} = (obj_i - \min_i)/(\max_i - \min_i) \tag{2}$$

where $obj_i$ is the objective value of the $i^{\text{th}}$ sample, and $\max_i$ and $\min_i$ are the maximum and minimum values of the initial samples. Then total objective function of the optimization can be calculated as

$$\begin{aligned} obj_{final} &= obj_{t\_ave} \times 0.1 + (1 - obj_{t\_ripple}) \times 0.4 \\ &\quad + (1 - obj_{THD}) \times 0.4 + (1 - obj_{cogging}) \times 0.1 \end{aligned} \tag{3}$$

where $obj_{t\_ave}$, $obj_{t\_ripple}$, $obj_{THD}$, and $obj_{cogging}$ are normalized average torque, torque ripple, B-EMF THD, and cogging torque value. In order to focus on reducing the pulsation characteristics, weights on the torque ripple and B-EMF THD are set as 0.4 and the target of the optimization is maximizing the $obj_{final}$.

As a result of design optimization, a robust global solution was derived. The variables of the GO initial model and the robust model are tabulated on Table 4, and the rotor configuration is shown in Fig. 11.

The performance comparison of the GO initial model and robust model is listed in Table 5. The average torque, torque ripple, B-EMF THD, and cogging torque, which are considered objectives, are 1.82%, −37.60%, −13.84%, and 29.36% improved, respectively. As the performances of the considered objectives of the robust model were improved compared with GO initial model, the applicability of the IMROA to the practical motor design optimization is verified.

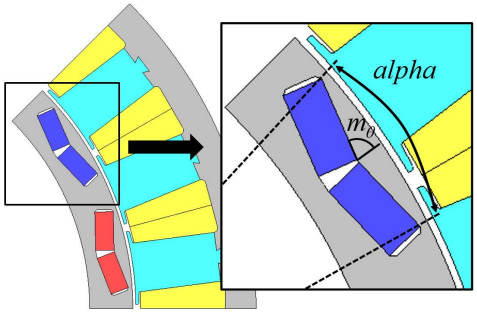


**FIGURE 10.** Design variables of the design optimization.

**TABLE 4.** Optimization result of the IMROA.

| Variable | GO initial model | Robust model |
|---|---|---|
| $m_\theta$ | 80.0 | 74.9 |
| *alpha* | 65.0 | 68.6 |

The effect of GO utilization and design optimization is tabulated in Table 2 and Table 5, respectively, and each method improves the performance of the IPMSM of the HEV application. To conduct the overall comparison, the analysis result comparison of the NO model and the robust model is listed in Table 6, and the waveform comparison of the

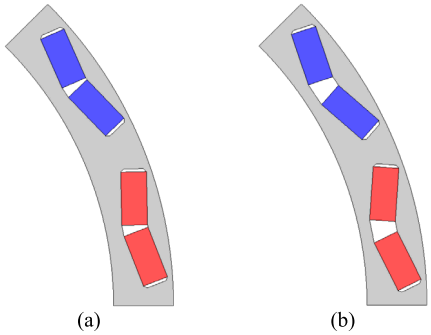


**FIGURE 11.** Comparison of the rotor figuration. (a) GO initial model. (b) Robust model.

**TABLE 5.** Performance comparison of the GO initial model and robust model.

| No-load | GO initial model | Robust model | Comparison |
|---|---|---|---|
| B-EMF [$V_{rms}$] | 159.53 | 156.98 | -1.60 [%] |
| B-EMF THD [%] | 11.56 | 9.96 | -13.84 [%] |
| Cogging torque [Nm] | 11.10 | 7.84 | -29.36 [%] |
| Iron loss [W] | 130.53 | 125.44 | -3.90 [%] |
| **Load** | **GO initial model** | **Robust model** | **Comparison** |
| Average torque [Nm] | 277.66 | 282.71 | +1.82 [%] |
| Torque ripple [%] | 20.72 | 12.93 | -37.60 [%] |
| Iron loss [W] | 412.41 | 426.24 | -3.35 [%] |
| Efficiency [%] | 96.65 | 96.68 | +0.03 [%] |

**TABLE 6.** Performance comparison of the NO model and robust model.

| No-load | NO model | Robust model | Comparison |
|---|---|---|---|
| B-EMF [$V_{rms}$] | 158.69 | 156.98 | -1.08 [%] |
| B-EMF THD [%] | 12.24 | 9.96 | -18.63 [%] |
| Cogging torque [Nm] | 10.33 | 7.84 | -24.12 [%] |
| Iron loss [W] | 174.96 | 125.44 | -28.30 [%] |
| **Load** | **NO model** | **Robust model** | **Comparison** |
| Average torque [Nm] | 263.19 | 282.71 | +7.42 [%] |
| Torque ripple [%] | 14.40 | 12.93 | -10.21 [%] |
| Iron loss [W] | 456.39 | 426.24 | -6.61 [%] |
| Efficiency [%] | 96.40 | 96.68 | +0.28 [%] |

NO and robust models are shown in Fig. 12. The magnetic flux density contour plot comparison is shown in Fig. 13. For the no-load analysis, the B-EMF THD was 18.63% reduced, cogging torque was 24.12% reduced, and iron loss was 28.30% reduced. The load condition results show 7.42% torque increase, 10.21% torque ripple reduction, 6.61% iron loss reduction, and 0.28% efficiency increase.

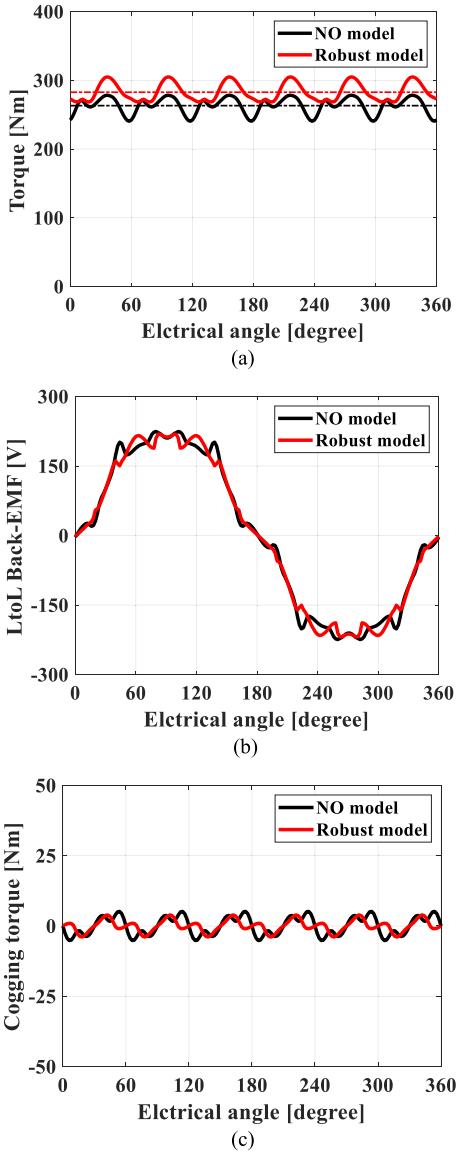


**FIGURE 12.** Waveform comparison of the NO model and robust model. (a) Torque waveform. (b) B-EMF waveform. (c) Cogging torque waveform.

The detailed comparison of the iron loss is conducted, and the results comparison is tabulated in Table 7. Especially for the stator teeth part, where the GO is applied, the iron loss was 41.45% and 30.34% reduced for the no-load and load condition. The reason for the low iron loss on

the stator teeth is superior B-W curve characteristics, shown in Fig. 1(b).

The robust model shows superior load and no-load performances compared with the NO model and the GO model. Moreover, the average torque, torque ripple, cogging torque, and B-EMF THD, which were objective functions, were 1.82%, 37.60%, 29.36%, 13.84% improved, respectively,

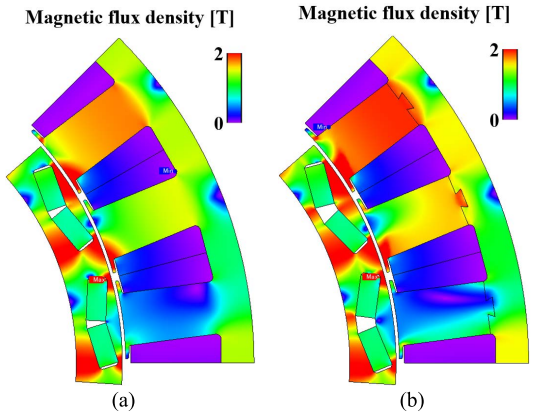


**FIGURE 13.** Load condition magnetic flux density contour plot. (a) NO model. (b) Robust model.

**TABLE 7.** Iron loss comparison of the NO model and robust model.

| No-load | NO model | Robust model | Comparison |
|---|---|---|---|
| Rotor core [W] | 8.29 | 7.27 | -12.34 [%] |
| Stator yoke [W] | 53.94 | 52.16 | -3.29 [%] |
| Stator teeth [W] | 112.73 | 66.01 | -41.45 [%] |
| Total [W] | 174.96 | 125.44 | -28.30 [%] |
| Load | NO model | Robust model | Comparison |
| Rotor core [W] | 62.53 | 73.84 | +18.10 [%] |
| Stator yoke [W] | 159.52 | 189.16 | +18.58 [%] |
| Stator teeth [W] | 234.34 | 163.24 | -30.34 [%] |
| Total [W] | 456.39 | 426.24 | -6.60 [%] |

by only changing the position of the magnet. Therefore, superior performance of the IMROA was validated, and the applicability of the IMROA to the practical electrical machine design optimization was conducted.

## IV. CONCLUSION

In this paper, the GO was applied at the IPMSM for HEV application. To utilize the superior effect of the GO, the GO was partially applied to the stator teeth, where the direction of the flux path is equal to the rolling direction of the GO, and the torque and iron loss was improved. For further performance enhancement of the IPMSM, design optimization was conducted by the proposed IMROA, which can consider robustness of the solution and reduce the calculation time. The IMROA derives a robust optimal solution with improved performance, and the applicability to the practical electrical machine design optimization was proved.

## REFERENCES

[1] C. Zhou, X. Huang, Z. Li, and W. Cao, "Design consideration of fractional slot concentrated winding interior permanent magnet synchronous motor for EV and HEV applications," *IEEE Access*, vol. 9, pp. 64116–64126, 2021.

[2] F. Lu, L. He, Q. Tan, and H. Zhou, "Efficiency optimization of IPOP DC/DC system for HEV," *IEEE Access*, vol. 9, pp. 31553–31561, 2021.

[3] O. Kolawole and I. Al-Anbagi, "Electric vehicles battery wear cost optimization for frequency regulation support," *IEEE Access*, vol. 7, pp. 130388–130398, 2019.

[4] J. Guo, H. Zhao, Z. Shen, A. Wang, L. Cao, E. Hu, Z. Wang, and X. Song, "Research on harmonic characteristics and harmonic counteraction problem of EV charging station," in *Proc. 2nd IEEE Conf. Energy Internet Energy Syst. Integr. (EI2)*, Oct. 2018, pp. 1–5.

[5] M. Zhu, X.-Y. Liu, L. Kong, R. Shen, W. Shu, and M.-Y. Wu, "The charging-scheduling problem for electric vehicle networks," in *Proc. IEEE Wireless Commun. Netw. Conf. (WCNC)*, Apr. 2014, pp. 3178–3183.

[6] Y. Cao, T. Wang, O. Kaiwartya, G. Min, N. Ahmad, and A. H. Abdullah, "An EV charging management system concerning drivers' trip duration and mobility uncertainty," *IEEE Trans. Syst., Man, Cybern., Syst.*, vol. 48, no. 4, pp. 596–607, Apr. 2018.

[7] J. Shen, S. Dusmez, and A. Khaligh, "Optimization of sizing and battery cycle life in battery/ultracapacitor hybrid energy storage systems for electric vehicle applications," *IEEE Trans. Ind. Informat.*, vol. 10, no. 4, pp. 2112–2121, Nov. 2014.

[8] B. Kou, L. Li, S. Cheng, and F. Meng, "Operating control of efficiently generating induction motor for driving hybrid electric vehicle," *IEEE Trans. Magn.*, vol. 41, no. 1, pp. 488–491, Jan. 2005.

[9] A. Gao, Z. Fu, and F. Tao, "Dynamic coordinated control based on sliding mode controller during mode switching with ICE starting for an HEV," *IEEE Access*, vol. 8, pp. 60428–60443, 2020.

[10] M. F. M. Sabri, K. A. Danapalasingam, and M. F. Rahmat, "A review on hybrid electric vehicles architecture and energy management strategies," *Renew. Sustain. Energy Rev.*, vol. 53, pp. 1433–1442, Jan. 2016.

[11] I. Urquhart, D. Tanaka, R. Owen, Z. Q. Zhu, J. B. Wang, and D. A. Stone, "Mechanically actuated variable flux IPMSM for EV and HEV applications," in *Proc. World Electr. Vehicle Symp. Exhib. (EVS)*, 2013, pp. 1–12.

[12] G. S. Lakshmi, "IPMSM for hybrid electric vehicle using DSP based three-level diode clamped inverter," in *Proc. IEEE Region 10 Symp. (TENSYMP)*, Jul. 2017, pp. 1–5.

[13] E. Sulaiman, T. Kosaka, and N. Matsui, "High power density design of 6-slot-8-pole hybrid excitation flux switching machine for hybrid electric vehicles," *IEEE Trans. Magn.*, vol. 47, no. 10, pp. 4453–4456, Oct. 2011.

[14] G. Lei, J. G. Zhu, Y. G. Guo, J. F. Hu, W. Xu, and K. R. Shao, "Robust design optimization of PM-SMC motors for six sigma quality manufacturing," *IEEE Trans. Magn.*, vol. 49, no. 7, pp. 3953–3956, Jul. 2013.

[15] H.-S. Kim and B.-I. Kwon, "Optimal design of motor shape and magnetisation direction to obtain vibration reduction and average torque improvement in IPM BLDC motor," *IET Electr. Power Appl.*, vol. 11, pp. 378–385, Mar. 2017.

[16] W. Ren, Q. Xu, Q. Li, and L. Zhou, "Reduction of cogging torque and torque ripple in interior PM machines with asymmetrical V-type rotor design," *IEEE Trans. Magn.*, vol. 52, no. 7, pp. 1–5, Jul. 2016.

[17] S. Magdaleno-Adame, T. D. Kefalas, A. Fakhravar, and J. C. Olivares-Galvan, "Comparative study of grain oriented and non–oriented electrical steels in magnetic shunts of power transformers," in *Proc. IEEE Int. Autumn Meeting Power, Electron. Comput. (ROPEC)*, Nov. 2018, pp. 1–7.

[18] K. Fujisaki and K. Fujitani, "Design of stator core shape of 'magnetic anisotropic motor,"' in *Proc. XX Int. Conf. Electr. Mach.*, Nov. 2012, pp. 183–189.

[19] E. A. Perigo and D. Tremelling, "Grain-oriented magnetic particles for energy applications," *IEEE Magn. Lett.*, vol. 9, pp. 1–4, 2018.

[20] T. Steinmetz, B. Cranganu-Cretu, and J. Smajic, "Investigations of no-load and load losses in amorphous core dry-type transformers," in *Proc. XIX Int. Conf. Electr. Mach. (ICEM)*, 2010, pp. 1–6.

[21] J. Seo, D. Woo, T. Chung, and H. Jung, "A study on loss characteristics of IPMSM for FCEV considering the rotating field," *IEEE Trans. Magn.*, vol. 46, no. 8, pp. 3213–3216, Aug. 2010.

[22] Z. Chen and G. Li, "A V type permanent magnet motor simulation analysis and prototype test for electric vehicle," *IEEE Access*, vol. 7, pp. 174839–174846, 2019.

[23] H. Chen and C. H. T. Lee, "Parametric sensitivity analysis and design optimization of an interior permanent magnet synchronous motor," *IEEE Access*, vol. 7, pp. 159918–159929, 2019.

[24] J. Hao, S. Suo, Y. Yang, Y. Wang, W. Wang, and X. Chen, "Optimization of torque ripples in an interior permanent magnet synchronous motor based on the orthogonal experimental method and MIGA and RBF neural networks," *IEEE Access*, vol. 8, pp. 27202–27209, 2020.

[25] J.-W. Jung, J.-P. Hong, and Y.-K. Kim, "Characteristic analysis and comparison of IPMSM for HEV according to pole and slot combination," in *Proc. IEEE Vehicle Power Propuls. Conf.*, Sep. 2007, pp. 778–783.

[26] C. Lai, G. Feng, K. Mukherjee, V. Loukanov, and N. C. Kar, "Torque ripple minimization for interior PMSM with consideration of magnetic saturation incorporating online parameter identification," *IEEE Trans. Magn.*, vol. 53, no. 6, pp. 1–4, Jun. 2017.

[27] J.-G. Lee, N.-W. Hwang, H.-R. Ryu, H.-K. Jung, and D.-K. Woo, "Robust optimization approach applied to permanent magnet synchronous motor," *IEEE Trans. Magn.*, vol. 53, no. 6, pp. 1–4, Jun. 2017.
[28] D. Lim, D. Woo, H. Yeo, S. Jung, J. Ro, and H. Jung, "A novel surrogate-assisted multi-objective optimization algorithm for an electromagnetic machine design," *IEEE Trans. Magn.*, vol. 51, no. 3, pp. 1–4, Mar. 2015.
[29] H. Yu, C. Y. Chung, K. P. Wong, H. W. Lee, and J. H. Zhang, "Probabilistic load flow evaluation with hybrid Latin hypercube sampling and Cholesky decomposition," *IEEE Trans. Power Syst.*, vol. 24, no. 2, pp. 661–667, May 2009.
[30] Y.-R. Kang, J.-C. Son, and D.-K. Lim, "Optimal design of IPMSM for fuel cell electric vehicles using autotuning elliptical niching genetic algorithm," *IEEE Access*, vol. 8, pp. 117405–117412, 2020.
[31] L. Fang, S.-I. Kim, S.-O. Kwon, and J.-P. Hong, "Novel double-barrier rotor designs in interior-PM motor for reducing torque pulsation," *IEEE Trans. Magn.*, vol. 46, no. 6, pp. 2183–2186, Jun. 2010.
[32] J.-C. Son, J.-M. Ahn, J. Lim, and D.-K. Lim, "Optimal design of PMa-SynRM for electric vehicles exploiting adaptive-sampling Kriging algorithm," *IEEE Access*, vol. 9, pp. 41174–41183, 2021.

**JI-CHANG SON** received the B.S. and M.S. degrees from the Department of Electrical, Electronic, and Computer Engineering, University of Ulsan, South Korea, in 2019 and 2021, respectively, where he is currently pursuing the Ph.D. degree.

**JI-YEON KIM** received the M.S. degree in mechanical engineering from the Department of Mechanical Engineering, Hanyang University, South Korea, in 2012. She is currently developing and researching motors for driving vehicles at Hyundai Motor Company.

**JAE-WAN CHOI** received the M.S. degree in electrical engineering from the Department of Electrical Engineering, Hanyang University, South Korea, in 2018. He is currently developing and researching motors for driving vehicles at Hyundai Motor Company.

**DONG-KUK LIM** received the B.S. degree in electrical engineering from Dongguk University, Seoul, South Korea, in 2010, and the Ph.D. degree in electrical engineering from Seoul National University, Seoul, in 2017, through the Combined Master's and Doctorate Program.

In 2017, he was with the Electrical Power Engineering Team, Hyundai Mobis Company, South Korea, as a Senior Research Engineer. He is currently an Assistant Professor with the Department of Electrical, Electronic, and Computer Engineering, University of Ulsan, South Korea. His research interest includes analysis and optimal design of electrical machines.

**HAN-KYEOL YEO** received the B.S. degree in electronic and electrical engineering from Sungkyunkwan University, Suwon, South Korea, in 2012, and the Ph.D. degree in electrical engineering from Seoul National University, Seoul, South Korea, in 2018, through the Combined Master's and Doctorate Program.

From 2018 to 2021, he was a Senior Research Engineer with the Advanced Electrification Development Team, Hyundai Motor Company, Hwaseong, South Korea. He is currently an Assistant Professor with the Division of Electrical and Electronic Engineering, The University of Suwon, Hwaseong. His research interest includes analysis and optimal design of electric machines.